



ELSEVIER

Contents lists available at ScienceDirect

## Cement and Concrete Composites

journal homepage: [www.elsevier.com/locate/cemconcomp](http://www.elsevier.com/locate/cemconcomp)

# Effect of morphological parameters of natural sand on mechanical properties of engineered cementitious composites

Hao-Liang Wu<sup>a,b</sup>, Jing Yu<sup>b,c</sup>, Duo Zhang<sup>b</sup>, Jun-Xing Zheng<sup>d</sup>, Victor C. Li<sup>b,\*</sup>

<sup>a</sup> Jiangsu Key Laboratory of Urban Underground Engineering & Environmental Safety, Institute of Geotechnical Engineering, Southeast University, Nanjing, 210096, China

<sup>b</sup> Department of Civil and Environmental Engineering, University of Michigan, Ann Arbor, MI, 48109, USA

<sup>c</sup> Department of Civil and Environmental Engineering, Hong Kong University of Science and Technology, Hong Kong, China

<sup>d</sup> Department of Civil, Construction and Environmental Engineering, Iowa State University, Ames, IA, 50014, USA

## ARTICLE INFO

## Keywords:

Engineered cementitious composite (ECC)

Local natural sand

Mechanical property

Morphological parameters

## ABSTRACT

Engineered Cementitious Composite (ECC) is an advanced construction material exhibiting tensile strain-hardening and multiple-cracking behavior. The tensile performance of ECC is known to be sensitive to the amount and size of sand used. Most studies on ECC have been performed with fine silica sand, while limited studies used coarser sand. However, the influence of morphological parameters of sand on the mechanical performance of ECC has not yet been explored, which is the focus of the present study. The morphological parameters (including particle roundness and sphericity) of sand were objectively determined using image analysis and computer algorithms, while the ECC compressive and tensile properties were experimentally measured. It was concluded that decreasing sand particle roundness and sphericity led to enhancements in compressive strength, ultimate tensile strength and tensile strain capacity of ECC. Gabbro sand, with the lowest roundness and sphericity among the four natural sand types studied, resulted in the best ECC mechanical properties. This natural sand can serve as an effective alternative to the typical manufactured fine silica sand used in ECC with reduced material cost and environmental impact. The findings of this study support the broader utilization of local natural sand in ECC in practical applications.

## 1. Introduction

Engineered Cementitious Composite (ECC) is a high-performance fiber reinforced cementitious composite that can enhance the resiliency and durability of structures [1,2]. The tensile strain capacity of ECC is typically over 3%, nearly 300 times that of conventional concrete [3,4], which can support infrastructure resiliency by suppressing fracture failure. Another unique feature of ECC is that the width of multiple cracks can be controlled to below 60 μm [5,6], contributing to low permeability and enhanced durability and self-healing capacity under cracked condition [4,7,8]. To achieve desirable mechanical performance, strength and energy criterions must be satisfied to ensure robust tensile strain-hardening and multiple-cracking based on the micro-mechanical model of ECC [1].

As an essential ingredient in typical ECC, sand has a significant impact on material workability, mechanical performance, shrinkage and material cost [4]. Particularly, the sand influences the fiber dispersion and tensile properties of ECC [9,10]. Improper sand size may

negatively affect fiber dispersion, leading to insufficient fiber bridging across one of the multiple crack planes [11] that may result in premature fracture localization, limiting the composite tensile strength and strain capacity [4]. Further, larger sand size may increase the tortuosity of crack propagation [10] and the effective matrix fracture toughness  $K_m$  which is unfavorable to flat crack propagation necessary for the formation of multiple cracking and high tensile ductility [4]. Typically, the average diameter of 60–110 μm is used in ECC [12–16].

Crushed sand and gravel sand with relatively larger size have also been explored to make ECC. Sahmaran et al., [9], Choi et al., [17] and Paul and van Zijl [18] successfully used 1.19–2.5 mm sand with to produce ECC with 28-day tensile strain capacity and tensile strength up to 1.96–3.04% and 3.07–4.28 MPa, respectively. Huang et al. [10] used the coarser iron ore tailing with 425 μm to replace the silica sand, and achieved a 28-day tensile strength at around 5.6 MPa and tensile strain capacity up to about 2.8%. Further, previous studies have also demonstrated that using local natural sand as an alternative to silica sand can reduce primary energy consumption, CO<sub>2</sub> emissions and

\* Corresponding author.

E-mail addresses: [wuhaoliang90@163.com](mailto:wuhaoliang90@163.com) (H.-L. Wu), [ceyujing@ust.hk](mailto:ceyujing@ust.hk) (J. Yu), [duzhang@umich.edu](mailto:duzhang@umich.edu) (D. Zhang), [junxing@iastate.edu](mailto:junxing@iastate.edu) (J.-X. Zheng), [vcli@umich.edu](mailto:vcli@umich.edu) (V.C. Li).

<https://doi.org/10.1016/j.cemconcomp.2019.04.007>

Received 26 November 2018; Received in revised form 1 March 2019; Accepted 7 April 2019

Available online 11 April 2019

0958-9465/ © 2019 Elsevier Ltd. All rights reserved.

transportation cost [19,20].

In spite of prior studies on the effects of sand type and sand size on the ECC's mechanical performance, the effects of morphological parameters (i.e., roundness and sphericity) of sand have not received much attention. In conventional concrete, the morphological parameters of sand are known to significantly influence the interfacial transition zone [21–23]. The presence of sand with smooth surface lead to a weaker interfacial transition zone, which can impair the compressive strength and matrix fracture toughness  $K_m$  [24]. The matrix fracture toughness  $K_m$  is one of the crucial parameters to attaining strain hardening behavior in ECC. Hence, it is necessary to investigate the effects of sand's morphological parameters on ECC's mechanical performance.

In this study, a comprehensive experiment was conducted to investigate the effect of sand's morphological parameters on the mechanical performance of ECC, in terms of compressive strength, tensile strength and ultimate tensile strain. The fiber dispersion coefficient of ECC was also analyzed. Empirical equations correlating sand morphological parameters and mechanical properties of ECC were established. Environmental impact and cost analyses were also performed and compared with conventional concrete. The findings of this study provide guidance in selecting suitable sand for ECC when options of local natural sand are available.

## 2. Materials and testing methods

### 2.1. Materials and mix proportion

The raw materials used in this study included Type I ordinary Portland cement (OPC), several types of local natural sand, ASTM Class F fly ash (FA), tap water, superplasticizers (SP) and polyvinyl alcohol (PVA) fibers. The detailed mix proportions are listed in Table 1.

Type I OPC from Lafarge (Southfield, MI) was used as a binder conforming to ASTM C150 [25] specifications. Class F fly ash from Headwaters Resources Inc. (Monroe, MI) was blended with OPC by a weight ratio of FA/OPC = 2.2. The SP produced from W.R. Grace & Co. (Columbia, MD) was used in preparation of all mixtures to maintain flowability and rheology of mix with a very low water/binder ratio. Four types of locally available natural sand, including Ottawa, crushed Gabbro, Michigan dune (MI), and 2NS, were sieved as per ISO 565/3310-1 standard sieves. To eliminate the effect of particle size on the mechanical performance of ECC, only sands with the particle size of 300–310  $\mu\text{m}$  were selected for this study. Therefore, the mean particle size for these four types of sand could be assumed as 305  $\mu\text{m}$ . The specific gravities for the four types of local natural sand were within 2.57–2.59  $\text{g}/\text{cm}^3$ . The four mixtures with different types of sand were denoted as Ottawa-ECC, Gabbro-ECC, MI-ECC and 2NS-ECC, as listed in Table 1. All mixes had 2.0 vol% of PVA fibers. The nominal physical

properties of PVA fibers are list in Table 2.

All mixtures were prepared using a 12-L Hobart mixer. The powder ingredients, including OPC, fly ash and sand, were first dry-mixed at 100 rpm for 2 min. Water and SP were then added into the dry mixtures and mixed at 150 rpm for 5 min to produce a consistent and uniform matrix. The PVA fibers were then added into the matrix and mixed at 150 rpm for additional 3 min. The fresh uniform matrix (fresh ECC without fibers) and mixtures were used to conduct Marsh cone test and mini-slump test, respectively.

### 2.2. Test methods

Marsh cone and mini-slump tests, following that described in Li and Li [11], were conducted to examine the influence of sand morphology on the workability of the fresh mixes. A plastic funnel with a capacity of 1700 mL (0.06  $\text{ft}^3$ ) and an internal orifice diameter of 20 mm (0.787 inches) was used to conduct Marsh cone test in this study. The cone was completely filled with matrix and the bottom outlet was then opened, allowing the matrix to flow out. The Marsh cone flow time of matrix was the elapsed time in seconds between the opening of the bottom outlet and the time when all uniform matrix flow through the cone. In the mini-slump flow deformation test, a truncated cone mold with a diameter of 100 mm (3.94 inches) at the bottom and 70 mm (2.76 inches) at the top and a height of 60 mm (2.36 inch) was placed on a smooth plate, filled with ECC mixtures, and lifted upward. The slump flow deformation (pancake diameter of the self-consolidating mix) was recorded once the mixtures stopped flowing. To minimize the effect of all possible variations, the tests were repeated twice and the average of results was considered for each mixture.

After the workability measurements, the fresh ECC mixtures were then cast into stainless steel molds for compression and uniaxial tension tests. These specimens were set in air at a temperature of  $20 \pm 2^\circ\text{C}$  and relative humidity (RH) of  $65 \pm 2\%$  and were demolded after 24 h. The compression test was performed on three 50 mm  $\times$  50 mm  $\times$  50 mm cube specimens as per ASTM C109/C109 M [26] after 7-day and 28-day air curing (temperature =  $20 \pm 2^\circ\text{C}$ , RH =  $65 \pm 2\%$ ). The loading rate was  $0.34 \pm 0.07 \text{ MPa}/\text{s}$  ( $50 \pm 10 \text{ psi}/\text{s}$ ). The uniaxial tension test was performed on the dogbone-shaped specimens following the Japan Society of Civil Engineers (JSCE) method [27]. The dimension of the dogbone mold is shown in Fig. 1. Linear variable displacement transducers (LVDTs) were used to measure the tensile deformation. The tension test was conducted by the Instron all-electric dynamic test instrument (ElectroPlus E10000 Linear-Torsion) with 10-kN load capacity. The dogbone specimens were gripped using wedge action on their slanting edges. Sufficient degree of freedom was provided in the grips to ensure the application of almost pure uniaxial tension along the longitudinal axis. Three samples for each mix were tested at a consistent

**Table 1**  
Materials mix proportions (by weight ratio) and flowability of ECC.

| Batch ID   | OPC | FA  | Sand | Water | SP    | PVA Fiber (vol%) | Flow time <sup>a</sup> (s) | Flow diameter <sup>b</sup> (mm) |
|------------|-----|-----|------|-------|-------|------------------|----------------------------|---------------------------------|
| Ottawa-ECC | 1   | 2.2 | 1.2  | 0.8   | 0.024 | 2                | 30.56                      | 212                             |
| Gabbro-ECC | 1   | 2.2 | 1.2  | 0.8   | 0.027 | 2                | 32.67                      | 203                             |
| MI-ECC     | 1   | 2.2 | 1.2  | 0.8   | 0.022 | 2                | 31.18                      | 196                             |
| 2NS-ECC    | 1   | 2.2 | 1.2  | 0.8   | 0.025 | 2                | 32.11                      | 200                             |

<sup>a</sup> Flow time measured using a modified Marsh cone [11].

<sup>b</sup> Flow diameter measured using a mini-slump cone.

**Table 2**  
Nominal properties of PVA fibers.

| Length (mm) | Diameter ( $\mu\text{m}$ ) | Elongation (%) | Density ( $\text{kg}/\text{m}^3$ ) | Young's modulus (GPa) | Tensile strength (MPa) |
|-------------|----------------------------|----------------|------------------------------------|-----------------------|------------------------|
| 8           | 39                         | 7              | 1300                               | 42.8                  | 1600                   |

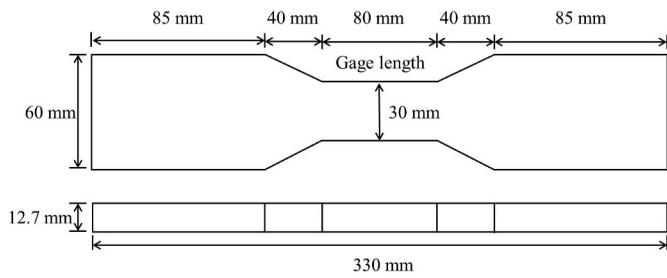


Fig. 1. Dimensions of the dogbone specimen for the uniaxial tension tests.

loading rate of 0.5 mm/min after 28-day air curing. After tension test, the tensile crack patterns were obtained by counting crack numbers and measuring crack width along the middle line of the specimen in the longitudinal direction.

After uniaxial tension test, fracture surfaces of the specimens were examined using a JEOL IT500 Scanning Electron Microscope (SEM) at 5 kV accelerating voltage. A 10 mm-thick sample (with a section area of  $30 \times 12.7 \text{ mm}^2$ ) from each dogbone specimen at the final failure section was cut perpendicular to the loading direction. Following Lee et al. [28], a fluorescence imaging technique was used to quantify the fiber distribution in this section. Without polishing, each sample from the four mixtures was examined under a fluorescence microscope (Nikon E-800) with an ultra-violet (UV) light source (Fig. 2a). The fluorescence image was then captured by a digital CCD camera (Q-imaging EXi 1394). For each cross section, the field of view of microscope was  $2.2 \times 1.7 \text{ mm}^2$  corresponding to  $1392 \times 1040$  pixels (Fig. 2b). Therefore, the whole cross-sectional area was divided into  $13 \times 7$  unit areas, and the number of fiber per unit area was counted. The fiber dispersion uniformity of the whole cross section was quantified by a fiber dispersion coefficient ( $\alpha$ ) [28]:

$$\alpha = \exp \left[ -\sqrt{\frac{\sum (x_i - \bar{x})^2}{n}} / \bar{x} \right] \quad (1)$$

where  $x_i$  is the number of fibers in the unit area  $i$ ,  $\bar{x}$  is the average number of fibers for a unit area, and  $n$  is the number of unit area.  $\alpha$  equaling to 0 implies all fibers are clumped together in one square, namely, no dispersion at all; whereas  $\alpha$  approaches 1 when the fiber dispersion reaches a uniform state.

### 3. Results and discussion

#### 3.1. Quantification of particle morphology and size for sand

The morphology of sand particle is usually quantified by sphericity ( $S$ ) and roundness ( $R$ ). Roundness was firstly proposed by Wadell

[29,30] to describe the sharpness of particle corners. As shown in Fig. 3a,  $R$  is defined as the ratio of the average radius of curvature of the particle's corners to the radius of the maximum inscribed circle (Eq. (2)). Sand particles with low angularity tend to have  $R$  approaching unity.

The sphericity  $S$  quantifies how close a particle's projected area is to a perfect circle. Based on the maximum projection of particle, Krumbein and Sloss [31] defined  $S$  as the ratio of particle width  $d_2$  to particle length  $d_1$ , as shown in Eq. (3). For perfect sphericity,  $S$  takes on a value of unity; for substantially elongated particles,  $S \ll 1$ .

$$R = \frac{\sum_{i=1}^N r_i / N}{r_{in}} \quad (2)$$

$$s = \frac{d_2}{d_1} \quad (3)$$

where  $r_i$  is the radius of the  $i$ -th corner circle;  $r_{in}$  is the radius of the maximum inscribed circle and  $N$  is the total number of corner circles. The schematically of roundness and sphericity of sand are shown in Fig. 3b.

Typical images for the Ottawa, Gabbro, MI, and 2NS sand are shown in Fig. 4. In these images, 200 particles are randomly selected from each type of sand and their shapes were evaluated by a computational technique [32]. The green circles are corner circles and red circles are maximum inscribed circle. The average  $R$  and  $S$  values of 200 particles were computed for each type of sand and shown in Fig. 4. All types of sand show similar  $S$  value (slightly lower for Gabbro), while  $R$  value ranges from 0.24 to 0.72 with Gabbro occupying the lowest value.

#### 3.2. Fresh property

The results of the workability test for specimens with different types of sand (with adjusted SP contents) are shown in Table 1. The dosage of SP to achieve almost identical fresh properties in ECC is plotted versus roundness and sphericity in Fig. 5, where the linear regressions using the least square method are also shown. The dosage of SP decreases with increasing roundness and sphericity of the local natural sand. This might be attributed to that sand with higher roundness and sphericity creates lower internal friction during mixing and results in better workability of ECC.

#### 3.3. Unconfined compressive strength

The 7-day and 28-day unconfined compressive strength (UCS) of different mixtures is summarized in Fig. 6. The 7-day UCS of Gabbro-ECC and 2NS-ECC could reach 39.8 MPa and 38.2 MPa, respectively. After 28-day curing, the UCS of Gabbro-ECC achieved 44.6 MPa, which was about 7.0% higher than that of 2NS-ECC. Compared with the UCS of Gabbro-ECC, the 7-day and 28-day compressive strengths of Ottawa-

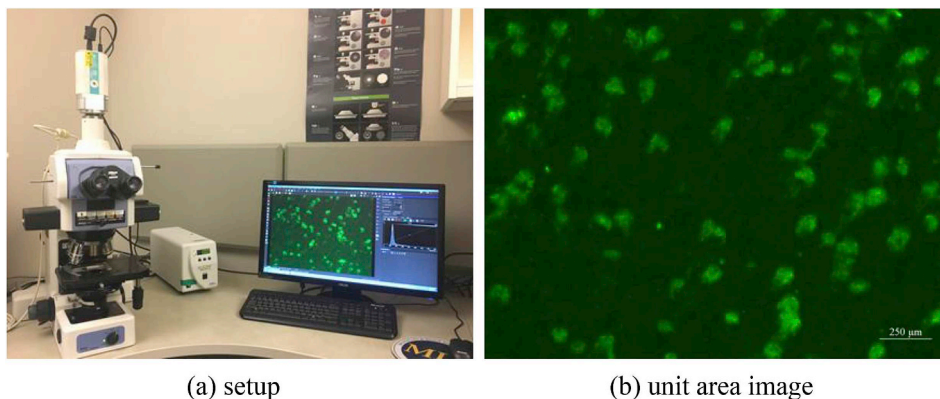


Fig. 2. Fluorescence microscope (a) setup and (b) an unit area image captured from a ECC cross section.

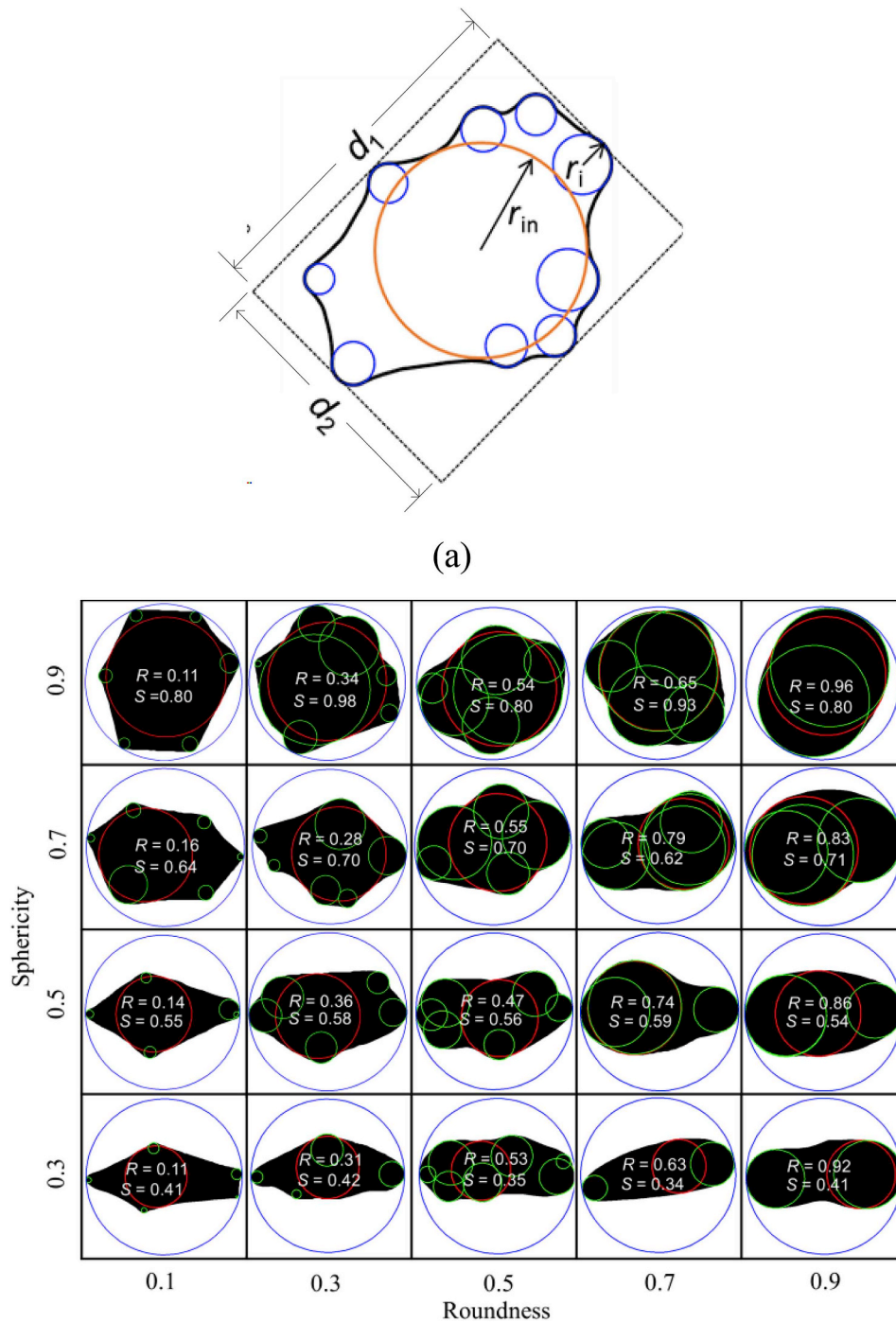


Fig. 3. Sand morphological characterization (a) schematically illustrated for roundness and sphericity (b) as computed by automated image technique.

ECC and MI-ECC are dramatically about 50% and 35% lower, respectively.

The strength of sand is rarely tested and generally does not influence the strength of conventional concrete as much as the strength of the paste and the paste-aggregate bond [33]. Hence, the focus here is on the sand size and morphological parameters on the UCS of ECC. As shown in Fig. 7a, the UCS of ECC in this study and additional data from the literature (Table 3) generally show a decreasing trend with increasing sand size for the same sand type.

A decreasing relationship can be found between UCS and roundness as well as sphericity (Fig. 7b–c). As expected, the increase in roundness and sphericity reduces the paste/aggregate contact surface area and weakens the interfacial transition zone, resulting in lower UCS [22,24].

Eq. (4) is a linear regression (with the least square method) of the data obtained, which is presented as a 3D surface in Fig. 7d.

$$UCS = -25.15R - 28.09S + 71.45, \quad r^2 = 0.89 \quad (4)$$

### 3.4. Tensile performance

The 28-day tensile stress-strain curves with different types of local natural sand are shown in Fig. 8, and the major characteristics are summarized in Table 4. Gabbro-ECC shows the best performance with average ultimate tensile strength (UTS) and tensile strain capacity (TSC) of 4.98 MPa and 1.88%, respectively. Ottawa-ECC, MI-ECC and 2NS-ECC show lower UTS and TSC compared with Gabbro-ECC. The

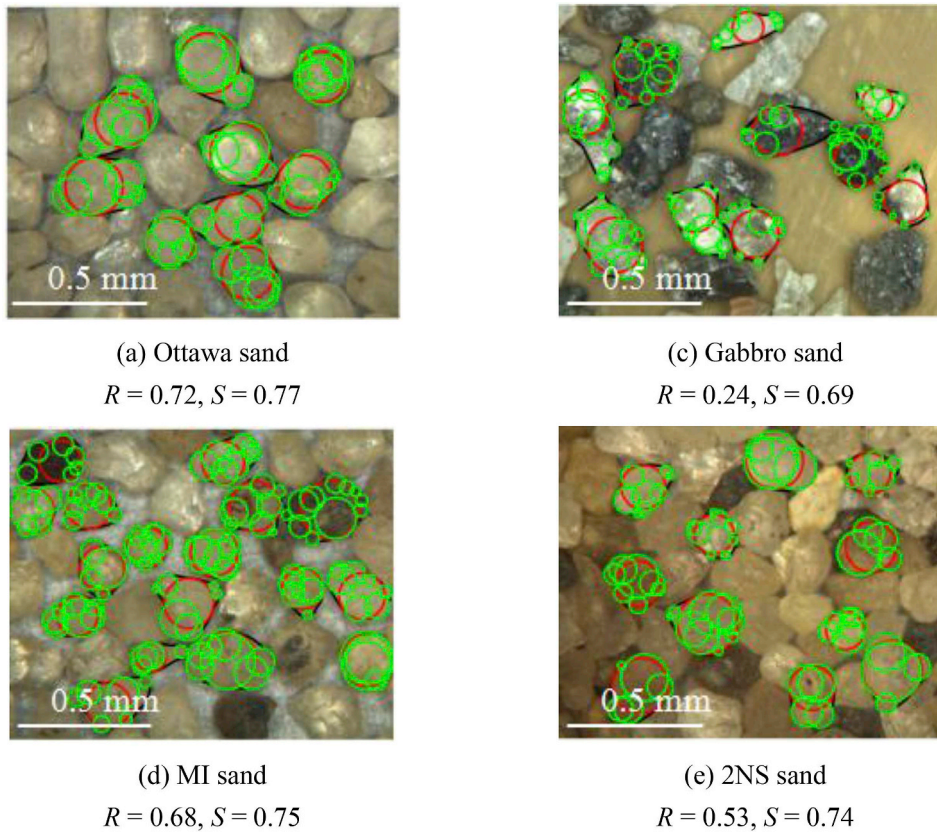


Fig. 4. The roundness and sphericity of sand in this study. Red circles represent inscribed circles and green circles represent corner circles. (For interpretation of the references to colour in this figure legend, the reader is referred to the Web version of this article.)

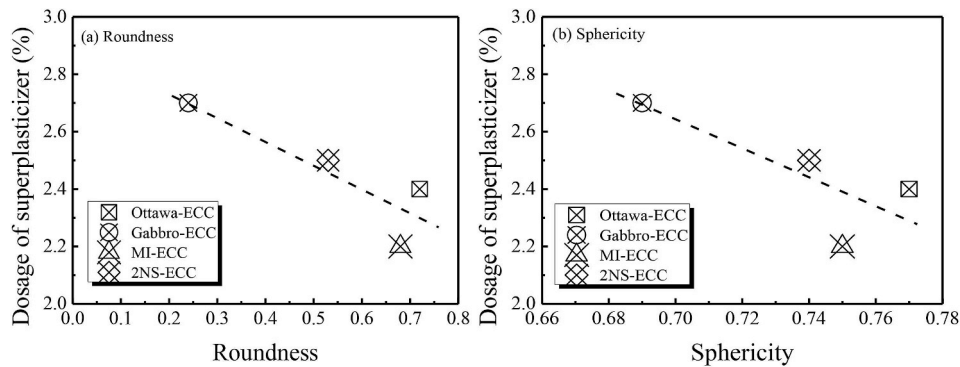


Fig. 5. Effect of (a) roundness and (b) sphericity on the dosage of superplasticizer to achieve almost identical fresh properties.

lower  $R$  and  $S$  lead to an increase in the first cracking strength, as summarized in Table 4. The multiple crack pattern of Gabbro-ECC was shown in Fig. 9.

The UTS varying with sand parameters are summarized in Fig. 10. The UTS decreases as the particle size increases from  $60\ \mu\text{m}$  to  $450\ \mu\text{m}$  (Fig. 10a). The UTS of ECC is governed by the minimum of the fiber-bridging capacities at all the multiple cracks, which is further dependent on the fiber dispersion, amongst other factors. Smaller aggregate size will likely promote the fiber dispersion uniformity and enhance the UTS of ECC. It is also observed that the UTS decreased with increasing roundness and sphericity for ECC with the same sand size ( $305\ \mu\text{m}$ ) (Fig. 10b–c). The mechanism behind this is further discussed in Section 3.4. Eq. (5) is a linear regression (with the least square method) of the data obtained, which is presented as a 3D surface in Fig. 10d.

$$UTS = -1.31R - 7.23S + 10.48, \quad r^2 = 0.75 \quad (5)$$

A decreasing linear relationship between TSC and sand size was found (Fig. 11a). It has been reported that the matrix fracture toughness increases with the aggregate size [35,36] due to the increase in crack propagation tortuosity. The increase in matrix toughness reduces the margin between the first-cracking strength and the ultimate tensile strength, leading to a reduction in tensile strain capacity (ref). This effect is amplified by the reduction in UTS as discussed previously. The relationship between  $R$ ,  $S$  and TSC is shown in Fig. 11b–c. For the same sand size, the TSC decreases with  $R$  and  $S$ , and the mechanism is further discussed in Section 3.4. Eq. (6) is a linear regression (with the least square method) of the data obtained, which is presented as a 3D surface in Fig. 11d.

$$TSC = -1.31R - 1.46S + 3.10, \quad r^2 = 0.82 \quad (6)$$

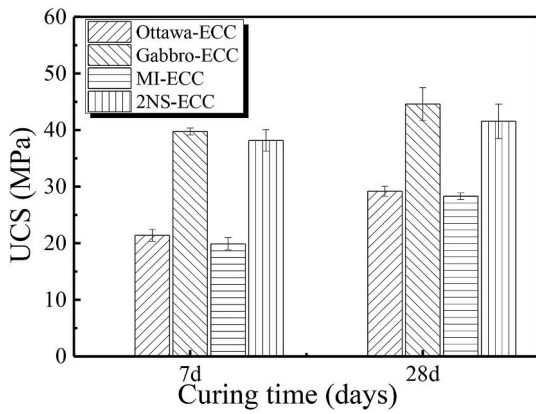


Fig. 6. Unconfined compressive strength (UCS) of ECC with different types of sand.

### 3.5. Underlying mechanisms

#### 3.5.1. Basic of micromechanical model

A previously developed micromechanical model [3,4] is used to gain insights into the relationship between the tensile performance of ECC and the morphological parameters of sand. According to the design theory of ECC, the first cracking strength  $\sigma_{fc}$  must not exceed the fiber

bridging capacity  $\sigma_0$  crossing that crack, as shown in Equation (7). Furthermore, the crack tip toughness  $J_{tip}$  must be less than the complementary energy  $J'_b$ , as shown in Equation (8). The  $\sigma(\delta)$  curve response the fiber bridging stress and crack opening widths of ECC.

$$\sigma_0 > \sigma_{fc} \tag{7}$$

$$J'_b \equiv \sigma_0 \delta_0 - \int_0^{\delta_0} \sigma(\delta) d\delta > J_{tip} \cong K_m^2 / E_m \tag{8}$$

where  $\sigma_0$  is the maximum bridging stress corresponding to the crack opening  $\delta_0$ ,  $K_m$  is the matrix fracture toughness, and  $E_m$  is the matrix Young's modulus. The delicate balance of matrix, fiber and matrix/fiber interfaces is necessary to obtain a robust tensile ductility.

#### 3.5.2. Fiber dispersion

Fig. 12a shows the fiber dispersion coefficients of ECC with different types of local natural sand. It was observed that the fiber dispersion coefficient decreases with increasing roundness and sphericity for ECC with the same sand size (305  $\mu\text{m}$ ) (Fig. 12b–c).

Fiber dispersion has a significant effect on the  $\sigma(\delta)$  curve, and in particular the maximum fiber-bridging stress  $\sigma_0$ . Poor fiber dispersion could result in a reduced effective  $V_f$  and then lower fiber-bridging stress  $\sigma_0$  at the final failure cross section [11], and a lower complementary energy  $J'_b$  as the  $\sigma(\delta)$  curve will be shifted downward. Thus, a lower fiber dispersion coefficient reduces the margin between  $\sigma_0$  and  $\sigma_{fc}$  (Eq. (7)) as well as  $J'_b$  and  $J_{tip}$  (Eq. (8)) and then leads to a lower

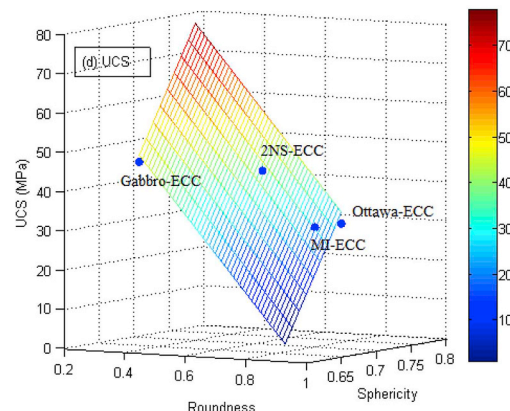
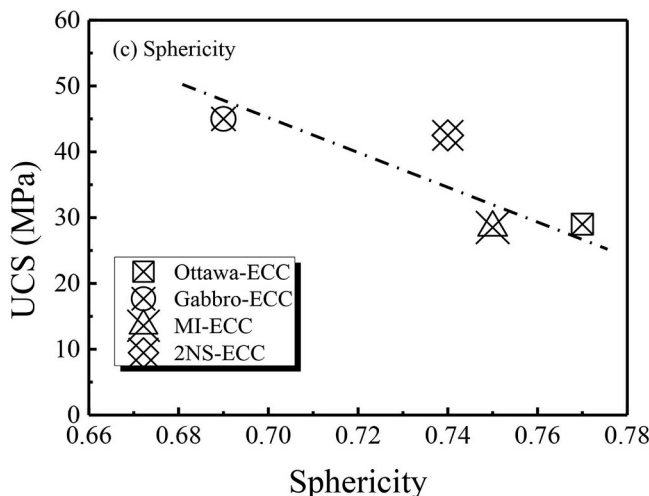
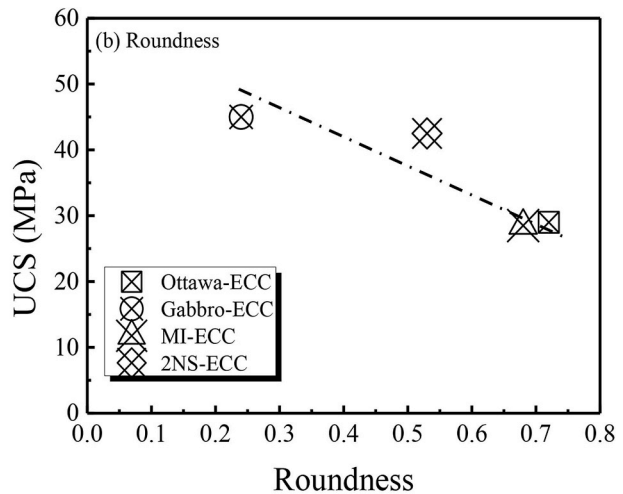
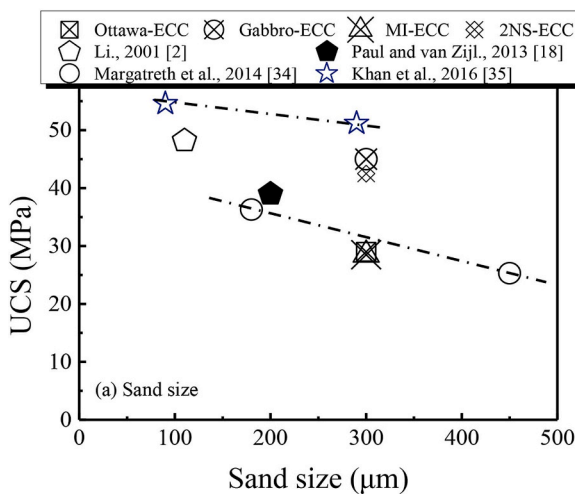
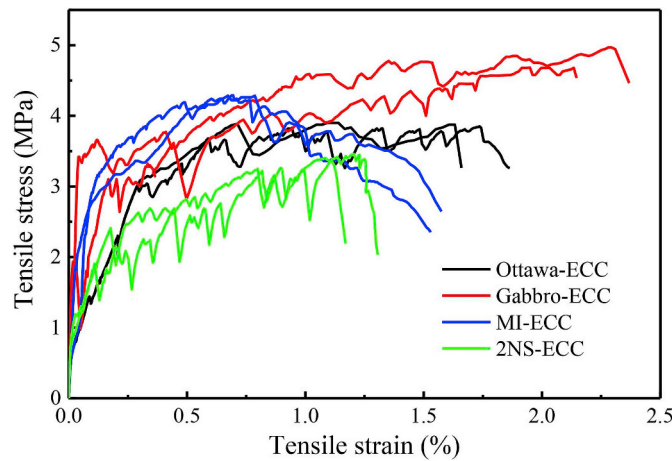


Fig. 7. Relation between unconfined compressive strength (UCS) and (a) sand size, (b) roundness and (c) sphericity; (d) 3D surface regression.

**Table 3**  
Summary of detailed information about ECC with natural sand.

| D <sup>a</sup> (μm) | UCS <sup>b</sup> (MPa) | UTS <sup>c</sup> (MPa) | TSC <sup>d</sup> (%) | Fiber       |            | Reference |
|---------------------|------------------------|------------------------|----------------------|-------------|------------|-----------|
|                     |                        |                        |                      | length (mm) | Volume (%) |           |
| 110                 | 48.20                  | 4.18                   | 3.16                 | 8           | 2.0        | [2]       |
| 180                 | 36.27                  | 2.12                   | 2.98                 | 12          | 2.5        | [34]      |
| 450                 | 25.25                  | 1.92–2.12              | 2.10                 | 12          | 2.5        | [34]      |
| 90                  | 54.60                  | 10.02                  | 0.6                  | 12          | 2.2        | [35]      |
| 290                 | 51.20                  | 9.43                   | 0.8                  | 12          | 2.2        | [35]      |
| 236                 | 35.00                  | 3.15                   | 1.20                 | 12          | 2.0        | [18]      |

- <sup>a</sup> D = Average diameter of sand.
- <sup>b</sup> UCS = unconfined compressive strength.
- <sup>c</sup> UTS = ultimate tensile strength.
- <sup>d</sup> TSC = tensile strain capacity.



**Fig. 8.** Tensile stress-strain curves for different sand.

tensile strain capacity. Therefore, higher roundness and sphericity cause lower fiber dispersion uniformity in the cross section, and then result in lower TSC of ECC (Fig. 12a).

3.5.3. Micromechanical analysis

The mechanism of the effect of morphological parameters of sand on the compressive strength and tensile performance of ECC is summarized in Fig. 13, which is based on the micromechanical design theory of ECC as reported in detail by Li [38]. The following discussion is based on the precondition of using sand with almost identical particle size. Higher roundness and sphericity result in the weak interfacial transition zone [34,37], and diminish the matrix fracture toughness  $K_m$ . Further, lower roundness and sphericity result in a longer cracking path during the matrix cracking process and more significant fiber abrasion during fiber pull out (Fig. 14), which has a positive effect on the compressive strength, first cracking strength  $\sigma_{fc}$  (Table 4), fiber/matrix interfacial frictional bond  $\tau_0$  and slip-hardening performance. It should be pointed out that the improved fiber/matrix interfacial frictional bond is not so

high as to cause severe fiber rupture in the present study. In addition, the moduli of different sand used in this study are almost identical, and therefore the elastic moduli of matrices of different ECC (Table 1) are almost the same (Fig. 8). Hence, lower roundness and sphericity lead to increments in the fiber-bridging capacity  $\sigma_0$ , crack tip toughness  $J_{tip}$  as well as complementary energy  $J'_b$ . Though  $\sigma_{fc}$ ,  $\sigma_0$ ,  $J_{tip}$  and  $J'_b$  are all increased, sufficient  $\sigma_0/\sigma_{fc}$  and  $J'_b/J_{tip}$  were achieved in the systems, which resulted in better tensile performance of ECC in terms of tensile strength, ultimate tensile strain and crack control capacity (Table 4).

3.6. Environmental impact and economic comparison

To quantify the environmental impact, material sustainability indicators (MSIs) can be used, which are calculated based on the energy and material flow in the manufacturing process and expressed in terms of energy consumption, waste and pollutant releases [2,39,40]. Three major MSIs, energy consumption, carbon dioxide (CO<sub>2</sub>) emission and solid waste, are adopted in the present study. The energy intensity, CO<sub>2</sub>

**Table 4**  
Uniaxial tensile properties and residual crack patterns of ECC.

| Materials ID | First cracking strength, $\sigma_{fc}$ (MPa) | UTS (MPa)   | TSC (%)     | Avg. crack width (μm) | No. of cracks |
|--------------|--|-------------|-------------|-----------------------|---------------|
| Ottawa-ECC   | 1.72 ± 0.03                                  | 3.81 ± 0.04 | 1.45 ± 0.13 | 31.7                  | 28            |
| Gabbro-ECC   | 1.92 ± 0.05                                  | 4.98 ± 0.11 | 1.88 ± 0.21 | 27.3                  | 34            |
| MI-ECC       | 1.78 ± 0.06                                  | 4.15 ± 0.09 | 0.83 ± 0.11 | 24.4                  | 23            |
| 2NS-ECC      | 1.85 ± 0.08                                  | 3.38 ± 0.01 | 1.17 ± 0.02 | 25.8                  | 26            |

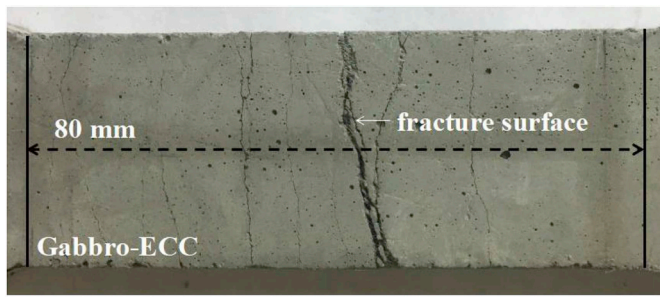


Fig. 9. Typical crack pattern Gabbro-ECC specimen.

emission, and material cost of each component are summarized in Table 5. The data are collected from the Portland Cement Association, a local contractor, publications in the literature and various material suppliers. In calculating solid waste, fly ash and local natural sand are assigned negative values because recycling removes them from the global waste flow.

The MSIs per unit volume of conventional concrete, a typical ECC mix denoted M45 (FA/OPC = 1.2) [4] and ECC with local natural sand consumes approximately 19.4% less energy and releases 26.6% less CO<sub>2</sub> emission than the typical ECC (M45). In terms of cost, a 13.3% reduction is achieved in natural sand ECC as compared to the typical ECC (M45). It should be pointed out that the reduction of transportation consumption was not considered in this study due to its dependence on transportation method. A more accurate assessment of environmental impact and cost should be based on the life-cycle analysis of a specific structure [4].

denotes total energy/CO<sub>2</sub> emission/cost of ECC,  $M_i$  and  $F_i$  denote energy/CO<sub>2</sub> emission/cost and fraction of mixing component  $i$ , respectively.

$$M_{total} = \sum M_i \times F_i \tag{9}$$

The energy consumption, CO<sub>2</sub> emission and cost of the typical ECC (M45) are 2.6, 1.6 and 4.1 times those of conventional concrete, respectively, due to the use of PVA fibers in the composite. The ECC with local natural sand consumes approximately 19.4% less energy and releases 26.6% less CO<sub>2</sub> emission than the typical ECC (M45). In terms of cost, a 13.3% reduction is achieved in natural sand ECC as compared to the typical ECC (M45). It should be pointed out that the reduction of transportation consumption was not considered in this study due to its dependence on transportation method. A more accurate assessment of environmental impact and cost should be based on the life-cycle analysis of a specific structure [4].

#### 4. Conclusions

This paper presents a comprehensive study on the influence of morphological parameters of sand on mechanical properties of Engineered Cementitious Composite (ECC). The roundness and sphericity of four types of natural sand, including Ottawa, crushed Gabbro,

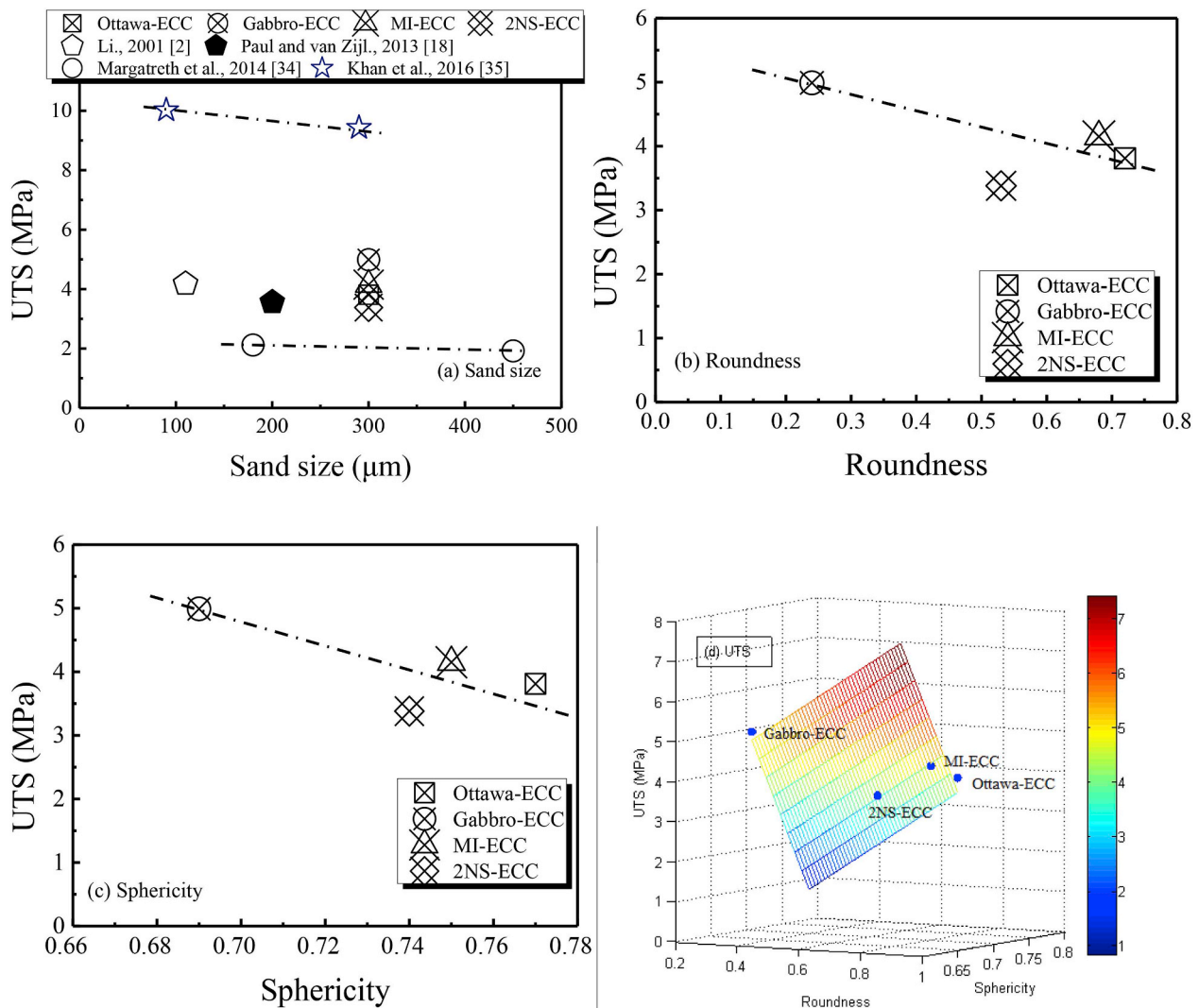


Fig. 10. Relation between ultimate tensile strength (UTS) and (a) sand size; (b) roundness; and (c) sphericity; (d) 3D surface regression.

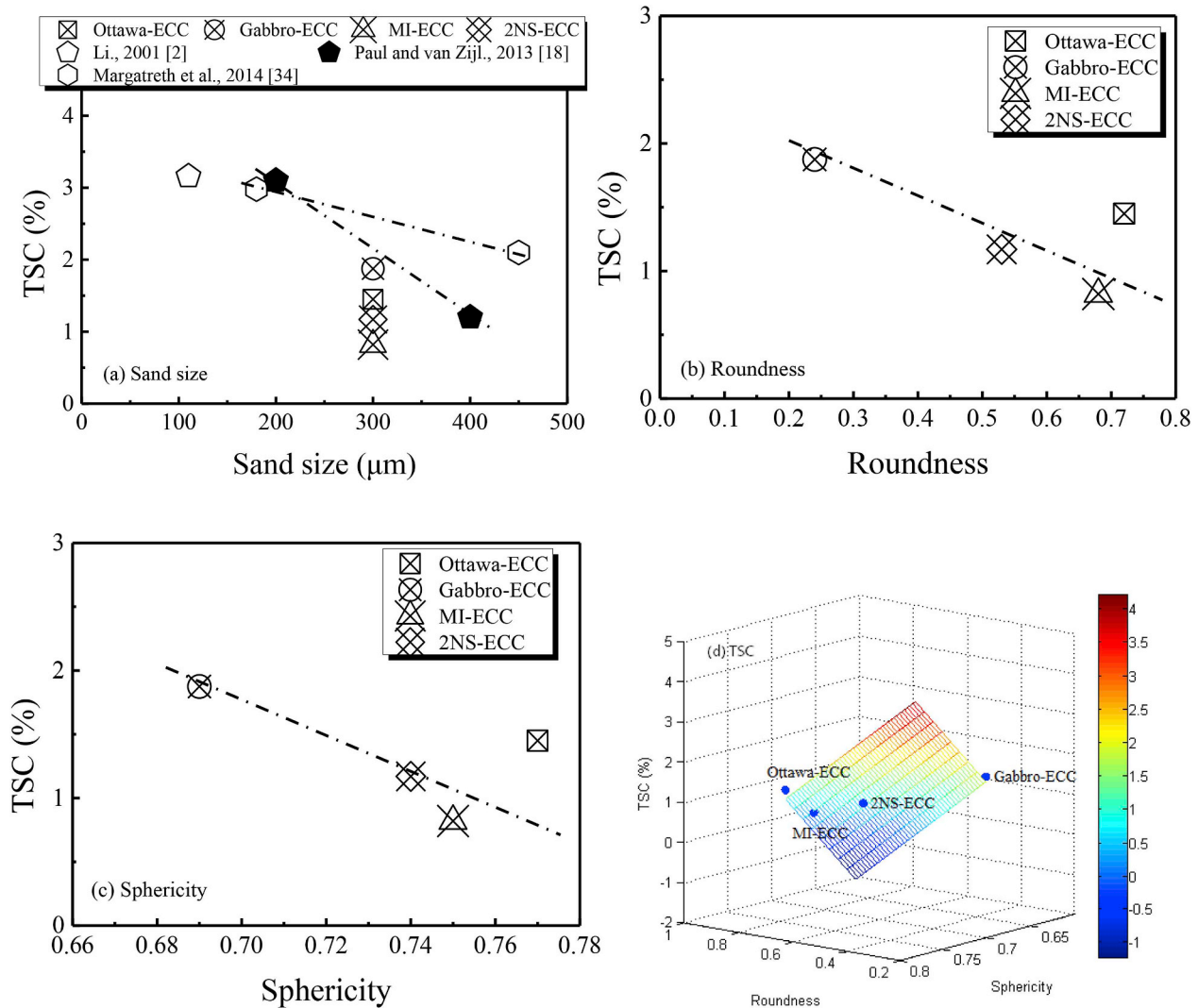


Fig. 11. Relation between tensile strain capacity (TCS) and (a) sand size; (b) roundness; and (c) sphericity; (d) 3D surface regression.

Michigan dune and 2NS were evaluated using a recently developed image-based computational morphological algorithm. Basic compressive and tensile properties of ECC with different types of natural sand were experimentally evaluated. Based on the results obtained from this study, the following conclusions can be drawn:

- (1) A strong correlation ( $r^2 = 0.75\text{--}0.89$ ) between the mechanical properties of ECC and morphological parameters (roundness and sphericity) of sand (with the same particle size) was discovered. Lower roundness and sphericity enhanced bonding between sand and binder material, resulting in a higher unconfined compressive strength. Further, a higher fiber dispersion uniformity was observed when sand with lower roundness and sphericity was used, resulting in a higher tensile strain capacity of ECC. Lower roundness and sphericity also enhanced the fiber/matrix interfacial frictional bond and the slip-hardening performance due to more severe fiber abrasion, leading to higher fiber-bridging capacity in the composite. Therefore, higher tensile strength and tensile strain capacity, as well as tighter crack width were attained in ECC using sand with lower roundness and sphericity.
- (2) The local natural sand studied exhibited sphericity of 0.69–0.77 and roundness of 0.24–0.72. With these four kinds of natural sand, ECC showed compressive strength of about 20–40 MPa at 7 days and

- around 30–45 MPa at 28 days, tensile strength of 3.4–5.0 MPa as well as ultimate tensile strain of 0.8–1.9% at 28 days.
- (3) The Gabbro-ECC, with the lowest sphericity and roundness among the four natural sand types tested, achieved the highest unconfined 28-day compressive strength (45 MPa) and exhibited the highest tensile strain capacity (1.9%) with strain-hardening and multiple-cracking characteristics. Compared to the typical ECC (M45) with fine silica sand (average size 110 μm), Gabbro-ECC shows reductions of 19.4%, 26.6% and 13.3% in embodied energy, CO<sub>2</sub> emission and material cost, respectively, despite having a lower strain capacity.
- (4) A decrease in sphericity and roundness of natural sands with the same average size required a higher dosage of superplasticizers to maintain similar workability in ECC.

Based on this study, local natural sand has the potential to be used to substitute manufactured sand and maintain tensile strain-hardening behavior in ECC. Sand characterized by low roundness and/or low sphericity is desirable for good tensile performance in ECC. The findings provide guidance for selecting sand in ECC when multiple options of local natural sand are available, and support the broader utilization of local natural sand in ECC in practical applications.

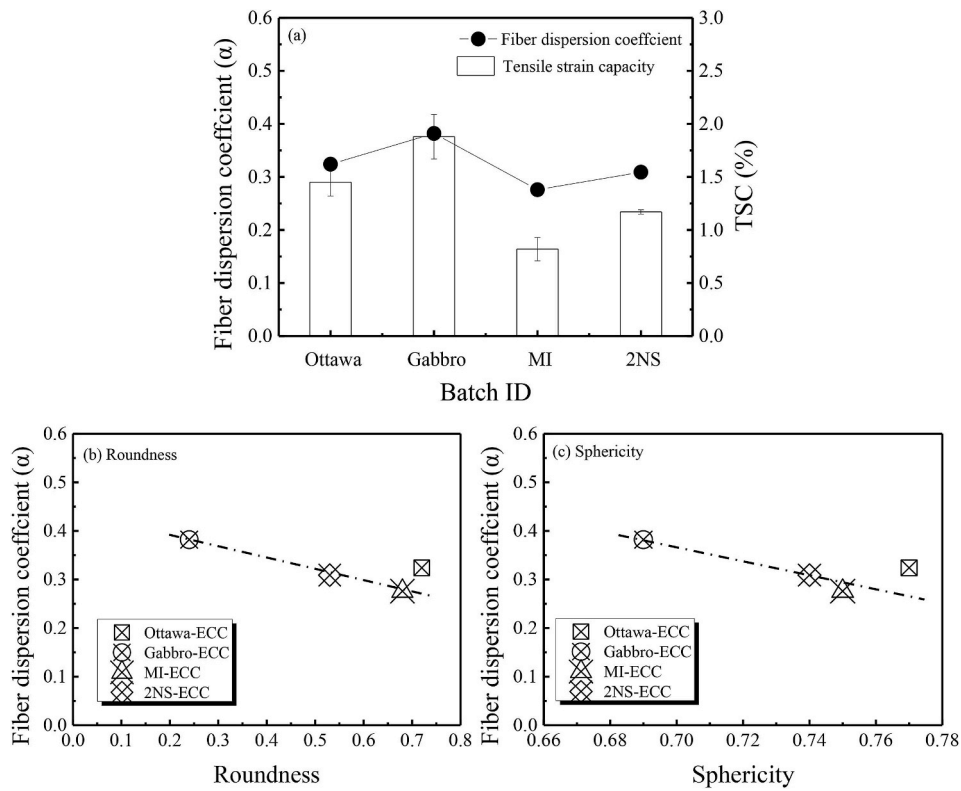


Fig. 12. Relation between fiber dispersion coefficient and (a) TSC; (b) roundness; (c) sphericity.

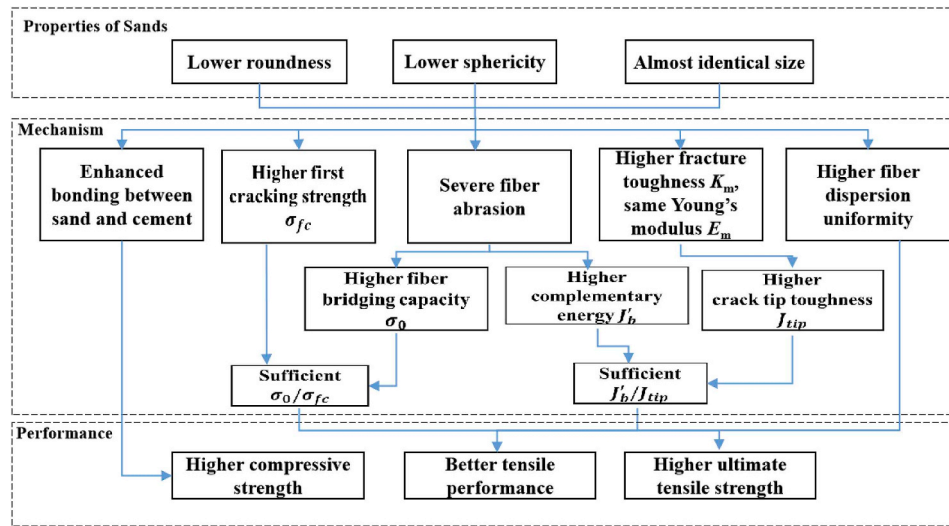


Fig. 13. Mechanism of the impact of morphological parameters of sand on compression and tension performance of ECC.

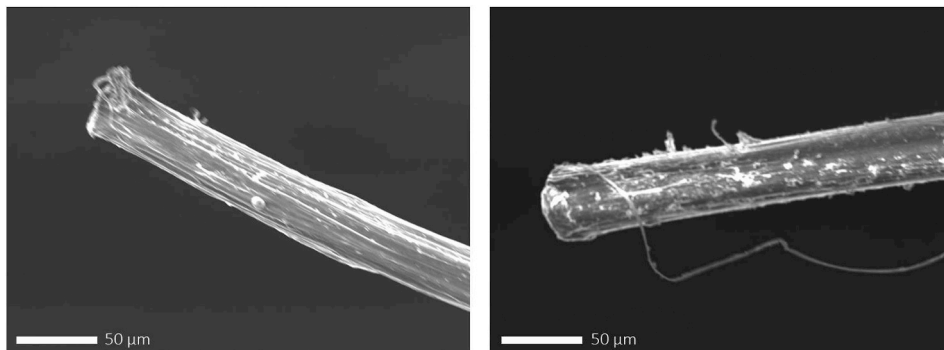


Fig. 14. SEM images showing fiber abrasion during pull-out from (a) Gabbro-ECC; (b) MI-ECC. The lower roundness of Gabbro sand causes more severe fiber abrasion shown as multiple grooves along the fiber axis.

**Table 5**  
Breakdown of embodied energy consumption, CO<sub>2</sub> emission and material cost for ECC component.

| Component        | Energy consumption (GJ/ton) | CO <sub>2</sub> emission (kg/ton) | Cost (USD/ton)      |
|------------------|-----------------------------|-----------------------------------|---------------------|
| Cement           | 4.5–6.6 <sup>a</sup>        | 870 <sup>a</sup>                  | 48 <sup>c</sup>     |
| Fly ash          | 0.85 <sup>b</sup>           | 27 <sup>b</sup>                   | 25.6 <sup>c</sup>   |
| Silica sand      | 0.067 <sup>a</sup>          | 23.28 <sup>d</sup>                | 63.9 <sup>e</sup>   |
| Local sand       | 0.008 <sup>c</sup>          | 3.50 <sup>c</sup>                 | 3.5 <sup>c</sup>    |
| Water            | 0                           | 0                                 | 7.0 <sup>e</sup>    |
| Superplasticizer | 35 <sup>d</sup>             | 1667 <sup>d</sup>                 | 1211.2 <sup>c</sup> |
| PVA Fiber        | 101 <sup>a</sup>            | 1710 <sup>d</sup>                 | 12670 <sup>e</sup>  |

<sup>a</sup> Data obtained from Ref. [41].

<sup>b</sup> Data obtained from Ref. [42].

<sup>c</sup> Data obtained from Ref. [43].

<sup>d</sup> Data obtained from Ref. [44].

<sup>e</sup> Market price subject to fluctuation (2018).

**Table 6**  
Comparison of MSIs and cost for conventional concrete, typical ECC and natural sand ECC.

| Materials             | Energy consumption (GJ/m <sup>3</sup> ) | CO <sub>2</sub> emission (kg/m <sup>3</sup> ) | Cost (USD/m <sup>3</sup> ) |
|-----------------------|---|---|----------------------------|
| Conventional concrete | 2.5 <sup>a</sup>                        | 373 <sup>a</sup>                              | 108 <sup>b</sup>           |
| Typical ECC (M45)     | 6.7                                     | 581   | 443                        |
| Natural sand ECC      | 5.4                                     | 426   | 384                        |

<sup>a</sup> Data obtained from Ref. [45].

<sup>b</sup> Data obtained from Ref. [38].

## Acknowledgments

Haoliang Wu appreciates the visiting PhD student grant sponsored by the Chinese Scholarship Council, and Jing Yu appreciates the Fulbright Scholar Program grant sponsored by the Bureau of Educational and Cultural Affairs United States and the Hong Kong Research Grants Council, for their visits in the Advanced Civil Engineering Materials Research Laboratory (ACE-MRL) at the University of Michigan. Haoliang Wu also thanks Mr. Shuangke Gou for his guidance on Matlab.

## References

- V.C. Li, On engineered cementitious composites (ECC), *J. Adv. Concr. Technol.* 1 (3) (2003) 215–230, <https://doi.org/10.3151/jact.1.215>.
- V.C. Li, T. Horikoshi, A. Ogawa, S. Torigoe, T. Saito, Micromechanics-based durability study of polyvinyl alcohol-engineered cementitious composite, *ACI Mater. J.* 101 (3) (2004) 242–248, <https://doi.org/10.14359/13120>.
- V.C. Li, From micromechanics to structural engineering—the design of cementitious composites for civil engineering applications, *J. Struct. Mech. Earth-Quake Eng.* 10 (1993) 37–48.
- V.C. Li, N. E. (Ed.), Engineered Cementitious Composites (ECC) - Material, Structural, and Durability Performance. Concrete Construction Engineering Handbook, CRC Press, 2008, <https://doi.org/10.1201/9781420007657.ch24>.
- V.C. Li, S. Wang, C. Wu, Tensile strain-hardening behavior of polyvinyl alcohol engineered cementitious composite (PVA-ECC), *ACI Mater. J.* 98 (6) (2001) 483–492, <https://doi.org/10.14359/10851>.
- M.D. Lepech, V.C. Li, Water permeability of engineered cementitious composites, *Cement Concr. Compos.* 31 (10) (2009) 744–753, <https://doi.org/10.1016/j.cemconcomp.2009.07.002>.
- V.C. Li, E.H. Yang, Self-healing in concrete materials, *Self-healing Materials*, Springer, Dordrecht, 2007, pp. 161–193, [https://doi.org/10.1007/978-1-4020-6250-6\\_8](https://doi.org/10.1007/978-1-4020-6250-6_8).
- J. Yu, H. Li, C.K.Y. Leung, X. Lin, J.Y.K. Lam, I.M.L. Sham, K. Shih, Matrix design for waterproof engineered cementitious composites (ECCs), *Constr. Build. Mater.* 139 (2017) 438–446, <https://doi.org/10.1016/j.conbuildmat.2017.02.076>.
- M. Sahmaran, M. Lachemi, K.M. Hossain, R. Ranade, V.C. Li, Influence of aggregate type and size on ductility and mechanical properties of engineered cementitious composites, *ACI Mater. J.* 106 (2009) 308–316, <https://doi.org/10.14359/56556>.
- X. Huang, R. Ranade, W. Ni, V.C. Li, Development of green engineered cementitious composites using iron ore tailings as aggregates, *Constr. Build. Mater.* 44 (2013) 757–764, <https://doi.org/10.1016/j.conbuildmat.2013.03.088>.
- M. Li, V.C. Li, Rheology, fiber dispersion, and robust properties of engineered cementitious composites, *Mater. Struct.* 46 (3) (2013) 405–420, <https://doi.org/10.1617/s11527-012-9909-z>.
- C.J. Adendorff, W.P. Boshoff, G.P.A.G. Van Zijl, Characterisation of crack distribution of Strain-Hardening Cement Composites (SHCC) under imposed strain, *Adv. Cem. Base Mater.* (2009) 215–221, <https://doi.org/10.1201/b10162-32>.
- F.H. Wittmann, T. Zhao, L. Tian, F. Wang, L. Wang, Aspects of durability of strain hardening cement-based composites under imposed strain, *Proceedings of the International Conference on Advanced Concrete Materials*, 2009, pp. 17–19, <https://doi.org/10.1201/b10162-27>.
- Z. Pan, C. Wu, J. Liu, W. Wang, J. Liu, Study on mechanical properties of cost-effective polyvinyl alcohol engineered cementitious composites (PVA-ECC), *Constr. Build. Mater.* 78 (2015) 397–404, <https://doi.org/10.1016/j.conbuildmat.2014.12.071>.
- S.H. Said, H.A. Razak, Structural behavior of RC engineered cementitious composite (ECC) exterior beam–column joints under reversed cyclic loading, *Constr. Build. Mater.* 107 (2016) 226–234, <https://doi.org/10.1016/j.conbuildmat.2016.01.001>.
- J. Yu, J. Yao, X. Lin, H. Li, J.Y. Lam, C.K.Y. Leung, I.M. Sham, K. Shih, Tensile performance of sustainable Strain-Hardening Cementitious Composites with hybrid PVA and recycled PET fibers, *Cement Concr. Res.* 107 (2018) 110–123, <https://doi.org/10.1016/j.cemconres.2018.02.013>.
- W.C. Choi, H.D. Yun, J.W. Kang, S.W. Kim, Development of recycled strain-hardening cement-based composite (SHCC) for sustainable infrastructures, *Compos. B Eng.* 43 (2) (2012) 627–635, <https://doi.org/10.1016/j.compositesb.2011.11.060>.
- S.C. Paul, G.P.A.G. van Zijl, Mechanically induced cracking behaviour in fine and coarse sand strain hardening cement based composites (SHCC) at different load levels, *J. Adv. Concr. Technol.* 11 (11) (2013) 301–311, <https://doi.org/10.3151/jact.11.301>.
- M. Sherif, K. Hossain, M. Lachemi, Structural performance of polymer fiber reinforced engineered cementitious composites subjected to static and fatigue flexural loading, *Polymers* 7 (7) (2015) 1299–1330, <https://doi.org/10.3390/polym7071299>.
- H. Ma, S. Qian, Z. Zhang, Z. Lin, V.C. Li, Tailoring engineered cementitious composites with local ingredients, *Constr. Build. Mater.* 101 (2015) 84–595, <https://doi.org/10.1016/j.conbuildmat.2015.10.146>.
- K.A. Alshibli, A.M. Druckrey, R.I. Al-Raoush, T. Weiskittel, N.V. Lavrik, Quantifying morphology of sands using 3D imaging, *J. Mater. Civ. Eng.* 27 (10) (2014), [https://doi.org/10.1061/\(asce\)mt.1943-5533.0001246](https://doi.org/10.1061/(asce)mt.1943-5533.0001246) 04014275.
- G.C. Cordeiro, L.M.S.C. de Alvarenga, C.A.A. Rocha, Rheological and mechanical properties of concrete containing crushed granite fine aggregate, *Constr. Build. Mater.* 111 (2016) 766–773, <https://doi.org/10.1016/j.conbuildmat.2016.02.178>.
- E. Hervé, S. Caré, J.P. Seguin, Influence of the porosity gradient in cement paste matrix on the mechanical behavior of mortar, *Cement Concr. Res.* 40 (7) (2010) 1060–1071, <https://doi.org/10.1016/j.cemconres.2010.02.010>.
- M.A. da Silva, M. Pepe, R.G.M. de Andrade, M.S. Pfeil, R.D. Toledo Filho, Rheological and mechanical behavior of High strength steel fiber-river gravel self-compacting concrete, *Constr. Build. Mater.* 150 (2017) 606–618, <https://doi.org/10.1016/j.conbuildmat.2017.06.030>.
- ASTM C150/C150M, Standard Specification for Portland Cement, (2016).
- ASTM C109/C109M, Standard Test Method for Compressive Strength of Hydraulic Cement Mortars, (2013).
- JSCE, Recommendations for Design and Construction of High Performance Fiber

- Reinforced Cement Composites with Multiple Fine Cracks (HPFRCC). Concrete Committee, Rokugo K. (Chair), Japan Society of Civil Engineers, 2008 March, 212.
- [28] B.Y. Lee, J.K. Kim, J.S. Kim, Y.Y. Kim, Quantitative evaluation technique of polyvinyl alcohol (PVA) fiber dispersion in engineered cementitious composites, *Cement Concr. Compos.* 31 (6) (2009) 408–417, <https://doi.org/10.1016/j.cemconcomp.2009.04.002>.
- [29] H. Wadell, Volume, shape and roundness of rock particles, *J. Geol.* 40 (5) (1932) 443–451, <https://doi.org/10.1086/623964>.
- [30] H. Wadell, Sphericity and roundness of rock particles, *J. Geol.* 41 (3) (1933) 310–331, <https://doi.org/10.1086/624040>.
- [31] W.C. Krumbein, L.L. Sloss, Stratigraphy and sedimentation, *Soil Sci.* 71 (5) (1951) 401, <https://doi.org/10.1097/00010694-195105000-00019>.
- [32] J. Zheng, R.D. Hryciw, Traditional soil particle sphericity, roundness and surface roughness by computational geometry, *Geotechnique* 65 (6) (2015) 494–506, <https://doi.org/10.1680/geot.14.p.192>.
- [33] S.W. Tabsh, A.S. Abdelfatah, Influence of recycled concrete aggregates on strength properties of concrete, *Constr. Build. Mater.* 23 (2) (2009) 1163–1167, <https://doi.org/10.1016/j.conbuildmat.2008.06.007>.
- [34] M.D.S. Magalhães, R.D. Toledo Filho, E.D.M.R. Fairbairn, Influence of local raw materials on the mechanical behaviour and fracture process of PVA-SHCC, *Mater. Res.* 17 (1) (2013) 146–156, <https://doi.org/10.1590/s1516-14392013005000163>.
- [35] M.I. Khan, G. Fares, S. Mourad, W. Abbass, Optimized fresh and hardened properties of strain-hardening cementitious composites: effect of sand size and workability, *J. Mater. Civ. Eng.* 28 (12) (2016), [https://doi.org/10.1061/\(asce\)mt.1943-5533.0001665](https://doi.org/10.1061/(asce)mt.1943-5533.0001665) 04016152.
- [36] S. Erdem, M.A. Blankson, Fractal–fracture analysis and characterization of impact-fractured surfaces in different types of concrete using digital image analysis and 3D nanomap laser profilometry, *Constr. Build. Mater.* 40 (2013) 70–76, <https://doi.org/10.1016/j.conbuildmat.2012.11.013>.
- [37] D.D. Cortes, H.K. Kim, A.M. Palomino, J.C. Santamarina, Rheological and mechanical properties of mortars prepared with natural and manufactured sands, *Cement Concr. Res.* 38 (10) (2008) 1142–1147, <https://doi.org/10.1016/j.cemconres.2008.03.020>.
- [38] V.C. Li, Tailoring ECC for special attributes: a review, *Int. J. Concr. Struc. Mater.* 6 (3) (2012) 135–144, <https://doi.org/10.1007/s40069-012-0018-8>.
- [39] H.L. Wu, D. Zhang, B.R. Ellis, V.C. Li, Development of reactive MgO-based Engineered Cementitious Composite (ECC) through accelerated carbonation curing, *Constr. Build. Mater.* 191 (2018) 23–31, <https://doi.org/10.1016/j.conbuildmat.2018.09.196>.
- [40] J. Yu, C.K.Y. Leung, Strength improvement of strain-hardening cementitious composites with ultrahigh-volume fly ash, *J. Mater. Civ. Eng.* 29 (9) (2017), [https://doi.org/10.1061/\(asce\)mt.1943-5533.0001987](https://doi.org/10.1061/(asce)mt.1943-5533.0001987) 05017003.
- [41] G.A. Keoleian, A. Kendall, J.E. Dettling, V.M. Smith, R.F. Chandler, M.D. Lepech, V.C. Li, Life cycle modeling of concrete bridge design: Comparison of engineered cementitious composite link slabs and conventional steel expansion joints, *J. Infrastruct. Syst.* 11 (1) (2005) 51–60, [https://doi.org/10.1061/\(asce\)1076-0342\(2005\)11:1\(51\)](https://doi.org/10.1061/(asce)1076-0342(2005)11:1(51)).
- [42] J. Wang, Y. Wang, Y. Sun, D.D. Tingley, Y. Zhang, Life cycle sustainability assessment of fly ash concrete structures, *Renew. Sustain. Energy Rev.* 80 (2017) 1162–1174, <https://doi.org/10.1016/j.rser.2017.05.232>.
- [43] Mineral Products Association, Carbon Management, <https://mineralproducts.org/sustainability/carbon-management.html>.
- [44] F. Pacheco-Torgal, Z. Abdollahnejad, S. Miraldo, M. Kheradmand, Alkali-activated Cement-Based Binders (AACBs) as Durable and Cost-Competitive low-CO<sub>2</sub> Binder Materials: Some Shortcomings that Need to Be Addressed, Butterworth-Heinemann, Oxford, UK, 2017, pp. 195–216, <https://doi.org/10.1016/b978-0-12-804524-4.00009-9>.
- [45] E.H. Yang, Y. Yang, V.C. Li, Use of high volumes of fly ash to improve ECC mechanical properties and material greenness, *ACI Mater. J.* 104 (6) (2007) 620, <https://doi.org/10.14359/18966>.